

# Yearbook

## 2015



**Institute of Technical Physics  
and Materials Science**

<http://www.mfa.kfki.hu/>

Hungarian Academy of Sciences  
Centre for Energy Research



## **Institute of Technical Physics and Materials Science**

*Director:* Prof. István Bársony, corr. member of HAS

*Address:* Konkoly-Thege Miklós út 29-33,  
H-1121 Budapest, Hungary

*Postal:* P.O.Box 49, H-1525 Budapest, Hungary

*Phone:* +36-1-392 2225

*Fax:* +36-1-392 2226

*E-mail:* [info@mfa.kfki.hu](mailto:info@mfa.kfki.hu)

*URL:* <http://www.mfa.kfki.hu/>

MTA EK MFA Yearbook 2015

*Editor:* Csaba S. Daróczy

*Published by:* MTA EK MFA, Budapest, Hungary, 2015

## HIGHLIGHTS

### Wafer-scale integration of piezoelectric nanowires

(EU FP7 collaborative project 611019: PiezoMAT<sup>1</sup>)

I. E. Lukács, N.Q. Khánh, R. Erdélyi, Zs. Baji, G. Battistig, and J. Volk

The EU project PiezoMAT proposes new technologies of high-resolution fingerprint sensors based on a matrix of interconnected piezoelectric nanowires (NWs). One of the three targeted chip concepts was realized by the MFA team. Here the integrated free standing vertical NWs are contacted individually at their stock with two metal wires to detect piezoelectricity induced signals between tensed and compressed sides of the NWs upon bending. As it was found by finite element analysis a nearly constant positive/negative stress is built up in the outer/inner side of the NW upon bending it by a lateral loading force directing to its tip (Figs. 1a and b). In contrast, the induced piezoelectric potential has a strong maximum at the bottom of the NW (Fig. 1c). The aim of this sensor concept is to detect this enhanced electrical signal with a pair of metal electrodes contacting the opposite sides of the NWs at their roots. Moreover, with an array of vertically integrated NWs, the distribution of the loading force can also be detected at a very high (>5000 dpi) lateral resolution.

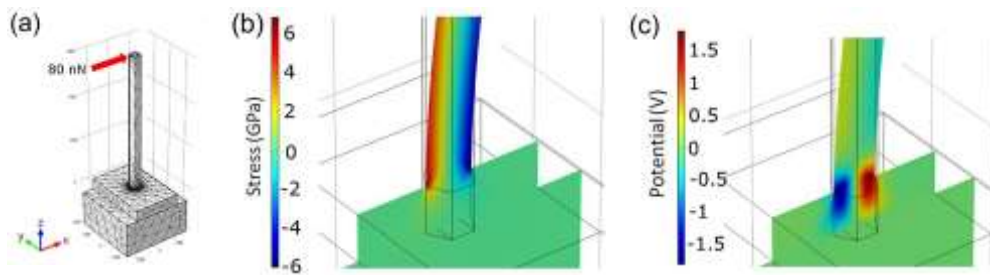


**Figure 1** Finite element analysis of NW/seed layer/substrate assembly showing the ideal meshing by triangular elements (a), cross-section of the  $\tau_{zz}$  component of the mechanical stress (b), and the electric potential distribution (c) for the bottom part of the bent NW at a loading force of 80 nN.

The optimization of the fabrication procedure was carried out through three stages, at first on small (10 mm × 10 mm) sapphire dices, then on 3" sapphire wafer, and at last on 3" Si wafer. The aim of the sapphire wafer is to realize 'ideal' monocrystalline ZnO NWs on epitaxial ZnO seed layer, whereas that of the Si wafer is to demonstrate

<sup>1</sup> FP7-ICT-2013-10- 611019 - High-resolution fingerprint sensing with vertical piezoelectric nanowire matrices (PiezoMAT), [www.piezomat.eu](http://www.piezomat.eu)

and test the feasibility of the process on standard Si technology. The optimized process flow consists of more than 25 technological steps, including five electron beam lithography (EBL) alignments. Hence the new Raith 150 EBL system of MFA (Fig. 2), enabling wafer scale processing of sub-20 nm sized patterns, played an essential role in this project. The fabrication process of the wafer had several challenges to be solved, such as the accurate (<50 nm) alignment of the EBL patterns; high quality metal lift-off process after EBL and photolithography; sample charging during EBL; mesa etching of ZnO seed layer; as well as the protection of ZnO mesa island against unwanted etchings.



**Figure 2** Raith 150 electron beam lithography system enabling nanopatterning of full wafers up to 6"-diameter. The system was successfully installed this year in the clean room of MEMS department and is being used in several projects.

The processed 3" Si wafer holds several chips (Fig. 3a) each of them having an active sensor array of  $8 \times 8$  individually contacted NWs in the center (Fig. 3b). Due to the

high quality ZnO seed layer deposited at the University of Leipzig (ULEI) the ZnO crystals show an excellent c-axis orientation even on the non-lattice matched SiO<sub>2</sub> covered Si wafer. Nevertheless these NW transducers are polycrystalline (Fig. 3d) in contrast to the ones grown on epitaxial ZnO/sapphire substrate (Fig. 3c). High resolution SEM images revealed that the piezocrystals were positioned to the readout contacts with sub-50 nm precision throughout the whole wafer (Fig. 3e).

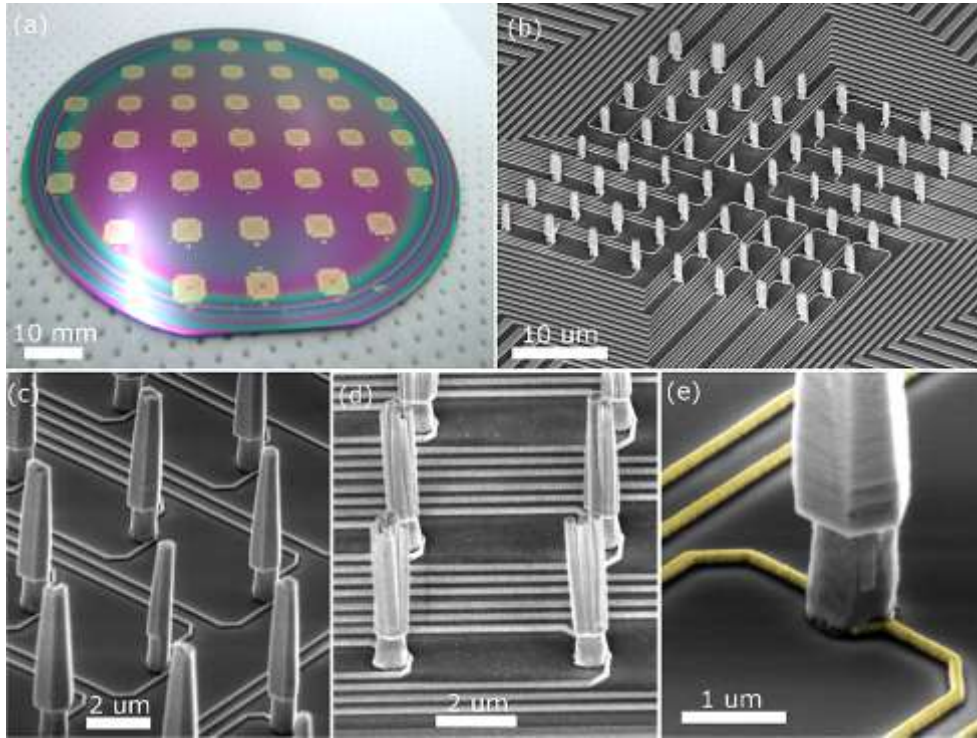


**Figure 3** On-chip integrated piezoelectric NWs. (a): Photo of Si wafer with NW chips, (b): SEM image of the  $8 \times 8$  NW array, (c and d, respectively): comparison of contacted ZnO NWs grown on sapphire and Si substrate, (e): high magnification SEM image of the contacted ZnO crystal where the read-out Au electrical lines are colored with yellow.

The electrical connections were verified by current-voltage (I-V) measurements using a probe station and negligible crosstalk was found between the separate circuits. The integrated NW chips are thus ready for the electromechanical characterizations which will be carried out in two main steps. At first bending experiments will be done on individual ZnO crystals with AFM and SEM micromanipulator tips in a highly controlled way. It will be followed by parallel detection when the whole array is imprinted with a soft stamp mimicking finger-print detection. Beside the targeted goal of PiezoMAT project, the fabricated chips are planned to be used for other purposes as well (e.g. for in-vitro cell monitoring), where very low lateral forces (1-1000 nN), and small movements are to be monitored in high resolution (>5000 dpi).



## ***Microtechnology Department***

**Head: Gábor BATTISTIG, Ph.D., senior research fellow**

### **Research Staff**

- Zsófia BAJI, Ph.D.
- István BÁRSONY, Member of HAS
- Gábor BATTISTIG, Ph.D.
- László DÓZSA, Ph.D.
- Csaba DÜCSŐ, Ph.D.
- Zoltán FEKETE, Ph.D. (on leave)
- Péter FÖLDESY, Ph.D.
- Péter FÜRJES, Ph.D.
- Zoltán HAJNAL, Ph.D.
- Nguyen Quoc KHÁNH, Ph.D.
- Zoltán LÁBADI, Ph.D.
- István LUKÁCS, Ph.D.
- György MOLNÁR, Ph.D.
- Andrea Edit PAP, Ph.D. (part time)
- Anita PONGRÁCZ, Ph.D.
- Vilmos RAKOVICS, Ph.D.
- István RÉTI, Ph.D.
- Attila Lajos TÓTH, Ph.D. (retired)
- János VOLK, Ph.D.
- Zsolt ZOLNAI, Ph.D.

### **Ph.D. students**

- Zsófia BÉRCES
- Zoltán SZABÓ
- Ferenc BÍRÓ
- Máté TAKÁCS
- Róbert ERDÉLYI
- Gergely MÁRTON
- Tamás KÁRPÁTI
- Eszter HOLCZER
- Eszter TÓTH

### **Technical Staff**

- János FERENCZ (engineer)
- Levente ILLÉS (engineer)
- Csaba LÁZÁR (engineer)
- Róbert HODOVÁN (engineer)
- András LŐRINCZ (engineer)
- Erika TUNYOGI (engineer, on leave)
- Katalin VERESNÉ VÖRÖS (engineer)
- György ALTMANN (technician)
- Gabriella BÍRÓ (technician)
- Sándor CSARNAI (technician)
- Tibor CSARNAI (technician)
- Magda ERŐS (retired)
- Károlyné PAJER (technician)
- Csilla ARIAS-SOTONÉ FARAGÓ (technician)
- Attila NAGY (technician)
- Magda VARGA (technician)

**The task of the Microtechnology Department is*****Fundamental research on:***

- sensing principles;
- novel materials and nanostructures;
- novel 3D fabrication techniques.

***Research and development of physical, chemical/biochemical sensors and integrated systems:***

- **MEMS** – R&D on micropellistor-type gas sensors, 3D force sensors, thermal sensors, CMOS compatible and related techniques.
- **BioMEMS** – Development of novel microfluidic systems, their application in new fields of biochemistry.
- **NeuroMEMS** – Development of Si- and polymer based sensors for biomedical applications with special focus on brain science.
- **NEMS** – Synthesis and characterization of quasi-one-dimensional semiconducting nanostructures, semiconductor nanodevices, their integration into functional sensors, optoelectronic and photovoltaic devices.

***Modelling, structural and device characterization methods available:***

- Electrical characterization;
- Thermo-mechanical characterization;
- Scanning Microprobes;
- Ion beam analysis methods;
- SEM, TEM, EDX;
- Spectroscopic Ellipsometry.

The Department runs two (300 m<sup>2</sup> + 160 m<sup>2</sup>) clean labs (Class 100-10000) comprising a complete Si-CMOS processing line and a mask shop, unique facility in Hungary. The technology allows to manufacture layers, patterned structures and devices with line resolution of 1 µm by optical and down to ≈10 nm by e-beam lithography on 3" and 4" Si and glass wafers.

***Competences*** (available also for our industrial and academic partners and customers):

- High temperature annealing, diffusion and oxidation;
- Ion implantation;
- Rapid Thermal Treatment;
- Low Pressure Chemical Vapor Deposition of poly-Si, SiO<sub>2</sub> and Si<sub>3</sub>N<sub>4</sub> layers;
- Low Temperature Chemical Vapor Deposition;
- Atomic Layer Deposition;
- Physical Vapor Deposition – Electron beam evaporation, DC and RF Sputtering;
- Reactive Ion Etching, Deep Reactive Ion Etching;

- Photolithography with back-side alignment and Nanoimprinting;
- E-beam lithography;
- Nanopatterning, deposition and etching by Focused Ion-Beam;
- Wafer-bonding;
- Wet chemical treatments;
- Electro-chemical porous Si formation;
- Molecular Beam Epitaxy of III-V compound semiconductors;
- Mask design, laser pattern generator;
- Polymer (PDMS, SU8, Polyimide) structuring by photolithography and micro-molding techniques;
- Chip dicing, packaging especially for sensor applications;
- Materials and structural analysis & characterization: SEM, FIB, EDX, Atomic Force Microscopy, Electrochemical Impedance Spectroscopy, Stylus Profiler;
- Electrical and functional modeling and characterization.



For detailed information please visit our web-site: [www.mems.hu](http://www.mems.hu)  
or contact us by e-mail: [dragon@mfa.kfki.hu](mailto:dragon@mfa.kfki.hu)



## **MEMS**

**Activity leader:** Cs. Dücső

**Group members:** Z. Baji, I. Bársony, G. Battistig, L. Dózsa, P. Földesy, P. Fürjes, Z. Hajnal, Z. Lábadi, G. Molnár, A.E. Pap, V. Rakovics, I. Réti, A.L. Tóth, Z. Zolnai, F. Biró, T. Kárpáti, M. Takács

### **Projects:**

- ENIAC CALL 2013-1 – “Intelligent Catheters in Advanced Systems for Interventions – INCITE”
- OTKA K109674 – “Graphen based terahertz modulators”
- OTKA PD116579 – “ZnO és Ga<sub>2</sub>O<sub>3</sub> nanostruktúrák készítése atomi rétegleválással”
- OTKA K112114 – “Kombinált mikro-nanotechnológiai eljárások és ellenőrzésük lokális analitikai technikákkal: a mintázatképzéstől az alkalmazások felé”
- KMR-12-1-2012-0107 – “Műszerfejlesztés talajvíz és egyéb vizek szénhidrogén szennyezettségének folyamatos megfigyelésére”
- KMR-12-1-2012-0226 – “Új generációs neutronos vizsgálóberendezések komponenseinek fejlesztése (2012-2015)”
- KMR\_12-1-2012-0031 – “Beágyazott informatikai rendszer fejlesztése energiapozitív közvilágítás optimalására”

### **Fine-tuning of gas sensitivity by modification of nano-crystalline WO<sub>3</sub> layer morphology**

Hexagonal WO<sub>3</sub> layers of different morphologies were deposited on micro-hotplate gas sensors and gas sensitivity for NH<sub>3</sub> was tested. The layers were synthesized by hydrothermal acidic precipitation method using different catalytic chemicals. Thin film sputtered layers were also deposited as reference material. WO<sub>3</sub> suspensions of quasi-equivalent quantity were dropped on the micro-hotplate for all the materials investigated. Additional ultrasonic agitation was introduced to destroy conglomerates of nano-crystals. If Na<sub>2</sub>SO<sub>4</sub> or K<sub>2</sub>SO<sub>4</sub> catalyst were added to the acidic solution of Na<sub>2</sub>WO<sub>4</sub>, ultrasonic treatment proved to be very effective and resulted in uniform sized individual WO<sub>3</sub> nano-rods of 80nm diameter. Addition of ZnSO<sub>4</sub> catalyst leads to disordered nano-fiber net with typical diameter of 70 nm. Ultrasonic agitation had no effect in case of NaCl catalyst and Zocher methods; thereby the formed WO<sub>3</sub> layers are composed of micrometer size conglomerates of 80-150 nm nano-rods. SO<sub>4</sub><sup>2-</sup> ions facilitate the formation of long crystallites.

Layers composed of individual nano-rods exhibit 2-5 times higher sensitivity up to 60ppm NH<sub>3</sub>, while layers of larger conglomerates show linear response in the 10-100ppm range. The size effect is explained by the comparable sizes of nano-wire

width and space charge layer at the solid-gas interface. This effect was also demonstrated by the sputtered thin films of different thicknesses.

$\text{Na}_x\text{WO}_3$  contamination deteriorates gas sensitivity. No relationship between specific surface and gas sensitivity could be detected.

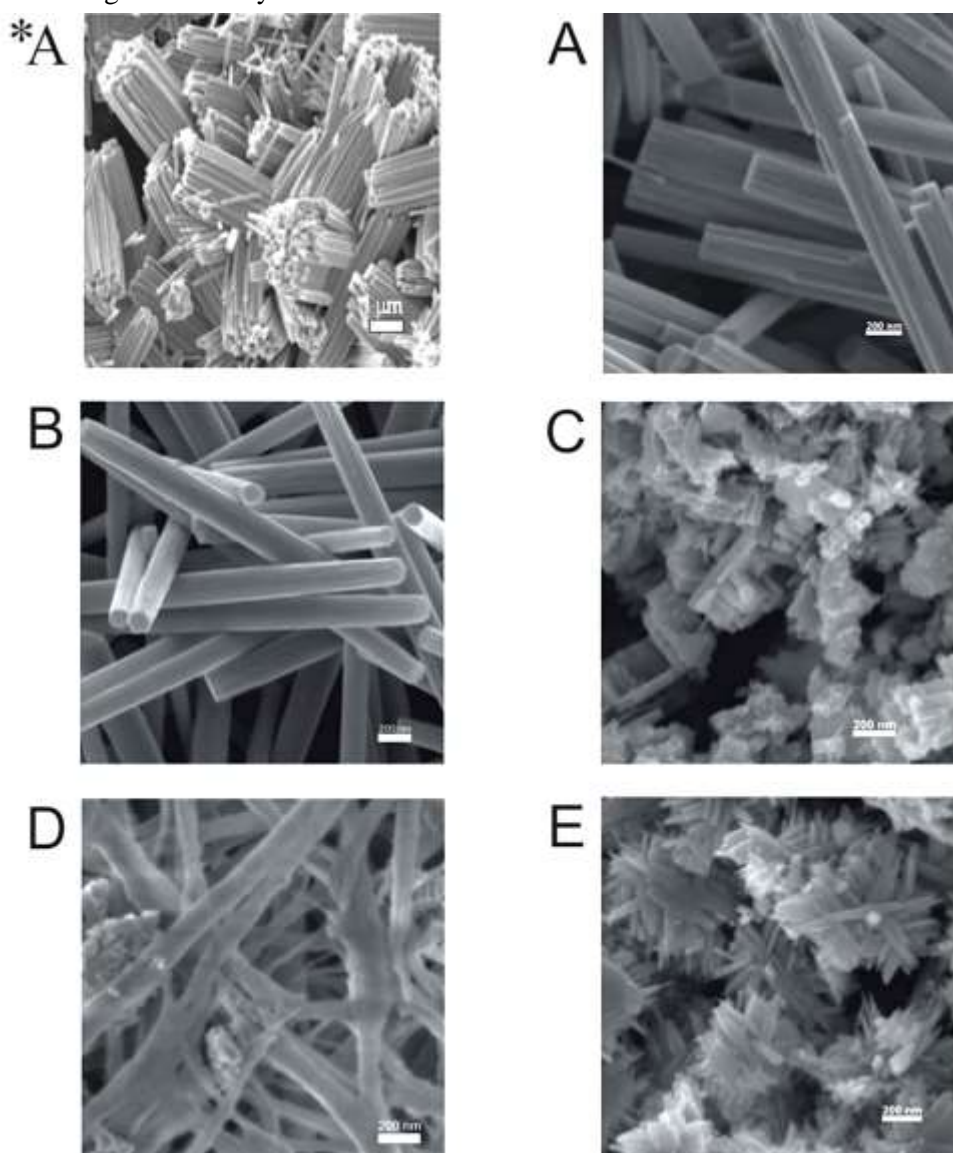


**Figure 1** SEM views of hydrothermally synthesised  $\text{WO}_3$  layers with different catalysts: (A\*):  $\text{Na}_2\text{SO}_4$  without ultrasonic treatment, (A):  $\text{Na}_2\text{SO}_4$  with ultrasonic treatment, (B):  $\text{K}_2\text{SO}_4$  with ultrasonic treatment, (C):  $\text{NaCl}$  with ultrasonic treatment, (D):  $\text{ZnSO}_4$  with ultrasonic treatment, (E): Zocher-method.

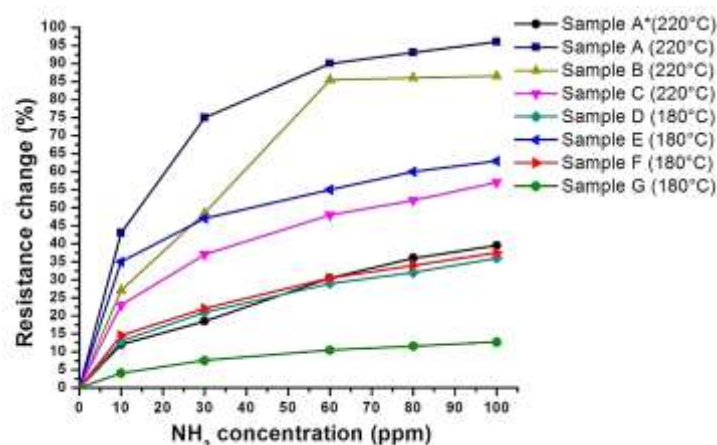


**Figure 2** Summary of sensor responses for 0-100ppm NH<sub>3</sub> in synthetic air.

The different characteristics of the alternatively processed WO<sub>3</sub> enables fine tuning of sensitivity. Combination of two layers also offers the possibility to expand measuring range.

### Wavelength conversion in GaInAsP/InP near infrared surface emitting diodes<sup>2</sup>

Quality control in food industry and clinical diagnostics requires powerful, versatile and relatively cheap spectrometers. Semiconductor light sources are characterized by small dimensions and low power consumption; therefore they can be suitable components in low price miniature devices. The only disadvantage of their application is that they are temperature sensitive and have a narrow spectrum. Infrared emitting diodes have 50 – 75 meV spectral bandwidths depending on the growth conditions. Thereby a series of spectrally tailored GaInAsP/InP surface emitting LED chips is required by micro-spectroscopy to cover the NIR (1000 – 1700 nm) wavelength range completely. Although these chips were developed in our lab and are efficiently applied by our partners, the need for spatially homogeneous, broad-spectrum and bright light sources drove us to develop a monolithic integrated NIR light source.

Present description demonstrates the results of a novel structure and its related technology to form single-chip broad or multi-peak spectrum LEDs. The output spectrum of the LED chip is substantially modified by introducing wavelength converter layers outside of the p-n junction of a normal LED structure. Light emitted from the active region is partly absorbed by the smaller band gap quaternary layers and re-emitted with smaller photon energy (Fig. 1). The emission spectrum and the

<sup>2</sup> Patent pending

light intensity can be tailored by the compositions, the thicknesses and number of the absorber layers. As an example, this absorption and re-emission process of the modified LED chips results in substantially broader two-peak emission spectrum (Fig. 2). A special advantage of the novel chip is that the spectral bandwidth of the device does not change with the driving current in the range of 10 mA to 100 mA. Moreover, the temperature dependence is also similar along the whole spectrum. More than 1 mW optical power can be obtained at 100 mA driving current and the corresponding operating voltage is 1.2 V.

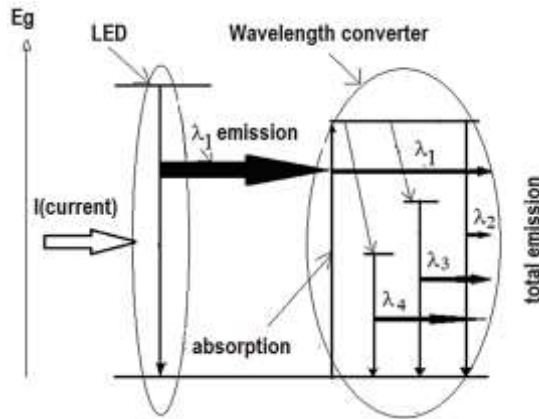


**Figure 1** Operation principle of the wide spectrum NIR light source.

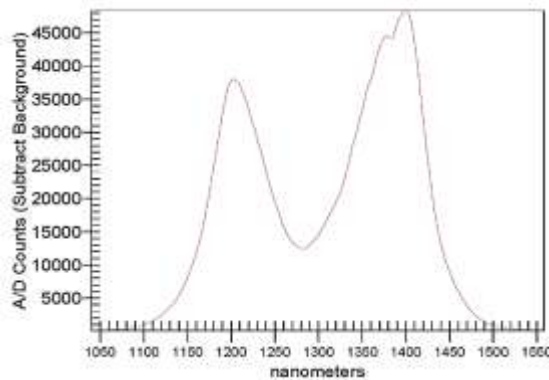


**Figure 2** Demonstration of the broad emission spectrum by a two-wavelength single-chip NIR light source. Peak at 1200 nm is from the LED, peak at 1400 nm is from the integrated single absorber layer light converter.

We have obtained even broader spectrum by inserting more additional different composition quaternary GaInAsP layers into the structure. These layers have lower band gap than the active and the first absorption layer. Sandwiching the absorber layer in additional narrow band gap GaInAsP layers the formed potential well enhance the direct recombination of the optically excited charge carriers. The device works similarly to phosphor conversion white LED structure, but it is more compact and stable, because all layers are lattice matched to the substrate. Its optimization is relatively easy if the light emitting layers are substantially thinner than the confining absorption layers. The novel one-chip LED structure provides point-like light source with broader spectra and facilitate the construction of low power miniaturized NIR

spectrometers. The multilayer structure enables to form stable light sources of emission spectrum tailored to any dedicated task.

### 3D force sensors for minimal invasive surgery applications

**Minimally invasive surgery** offers several advantages for the patient and also for the society. The quicker recovery and the smaller trauma are obviously essential for the patient, whereas the reduced hospitalization and recovery time helps the society to spend the medical costs more effectively.

**INCITE project** is intended to reveal and describe the advantages of the integration and application of various sensing capabilities in Minimal Invasive Surgery (catheter or surgery robot) systems. These subsystems are applicable to extend the functionality of the proposed medical systems to be applied by improving feedback for the operators and surgeons during the intervention. The future aim is to improve the functional characteristics, safety and standards of medical devices (catheters, robotic tools) applicable to minimal invasive cardiac intervention and surgery.



**Figure 1** Surgery robots (FRK) and the head where the force sensors will be integrated.

In order to improve the safety of the laparoscopic intervention the surgeon must get on-line information about the physical and chemical parameters during operation. The principal parameter required is the force as measured at different locations of the laparoscope head. Built inside the gripper the sensor can measure the strength of which the laparoscope holds the surgical tool. Placed on the tip the sensor can provide information about the hardness and surface roughness of the tissue the laparoscope touches (Fig. 1).

#### Design and fabrication of the 3D MEMS force sensors

3D force sensors were developed for the further integration in laparoscopic heads of surgery robots. The Si sensors operate with piezoresistive transduction principle by measuring the stress induced signals of the symmetrically arranged four piezoresistors in the deforming membrane. As the chip size has to be reduced to a few mm<sup>2</sup>, the conventional anisotropic alkaline etching technique was replaced by deep reactive ion etching (DRIE) for membrane formation. Besides, DRIE has no practical limitation in membrane geometry and offers the formation of monolith force transfer rod

protruding over the chip surface. SOI (silicon on insulator) wafers of appropriate device layer thickness provide the uniformity of membranes and reproducibility of the process.

According to the medical and functional requirements the MEMS sensors will be covered by biocompatible elastic polymer coating. Nevertheless, the elastomer drastically effect on the performance of the device. Therefore, the proposed sensor structures were modeled by coupled finite element simulation to determine the appropriate geometric parameters to meet the functional requirements. Sensors were covered with spherically shaped PDMS (polydimethylsiloxane) polymer and the effect of the elastic coating was also studied in terms of sensitivity and response time.

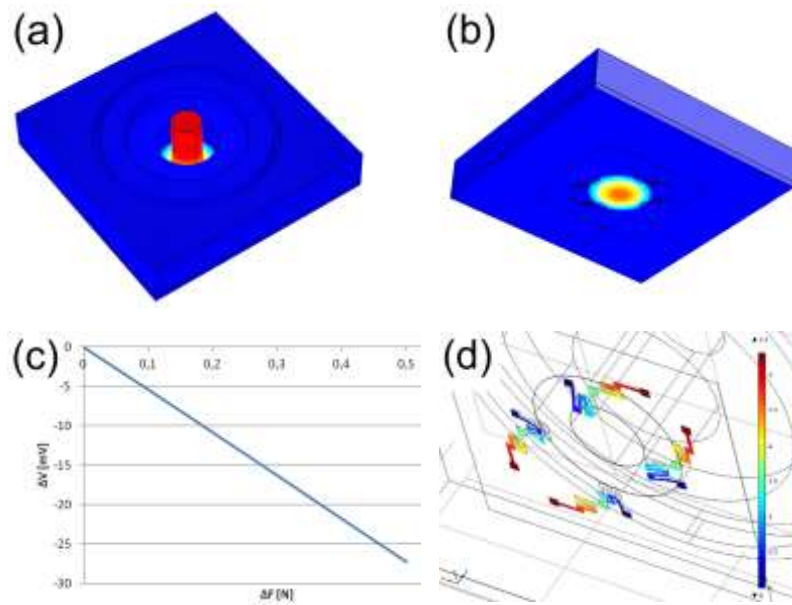


**Figure 2** Demonstration of the multiphysical coupled FEM simulation of the piezoresistive 3D force sensors: (a): membrane deformation, (b): stress distribution along the integrated piezoresistors, and (c,d): the (perpendicular) force dependent sensor signal.

Four half Wheatstone-bridges were formed on full Si membranes, each composed of two identical resistors and arranged such as to represent maximum out-of-balance voltages over mechanical deformation. The geometric design was aided by FEM calculations for any force range to be measured (Fig. 2).

The processed wafer was anodic bonded to boron glass to provide enhanced mechanical stability, cavity underneath the membrane and wire contacts for assembly. Processed chips (Fig. 3a) were mounted on TO8 headers or PCB header (Fig. 3b) for preliminary tests. In order to investigate the effect of the elastic coating, identical chips were covered by PDMS layer (Fig. 3c) and characterized as well.

The standard test includes the measurements of the four out-of-balance voltages over the applied force range in perpendicular directions of loads. (Fig. 4). The sensitivity is



heavily affected by the geometry and elasticity of the elastic coverage and this may result in up to 50-90% sensitivity loss.

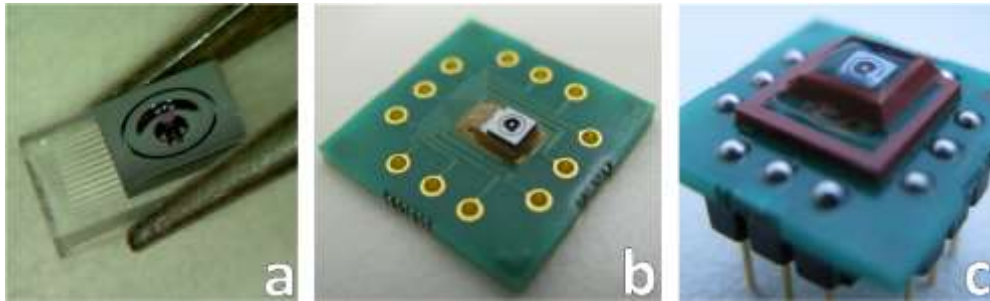


**Figure 3**  $2 \times 3 \text{ mm}^2$  full membrane force sensor chip (a), bare reference (b), and PDMS coated membrane type chips mounted on a specific PCB header for functional tests (c).

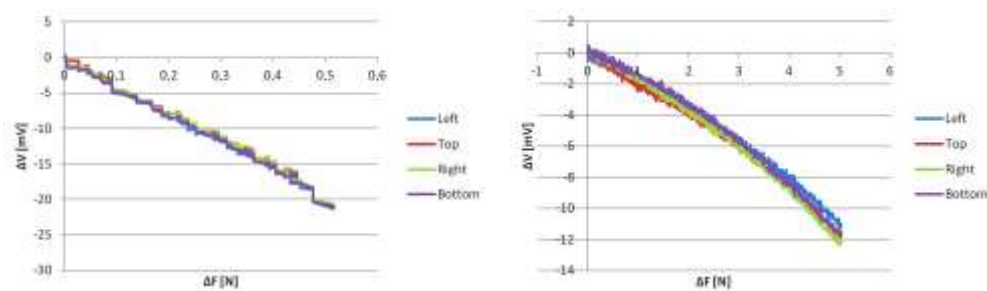


**Figure 4** Out-of-balance voltages of the four half Wheatstone-bridges for perpendicular loads. Bare chip (left), PDMS coated (right).

## Modeling and Simulation @ MEMS Lab

Finite Element Modeling (FEM) and multiphysics simulation, as implemented in COMSOL® have been the principal “workhorse” of semiconductor process workflow of the MEMS laboratory since many years. Several undergraduate and graduate thesis activities, related to deep brain electrodes, 3D (tactile) force sensors, numerous microfluidics devices were designed and optimized relying on insights gained from parametric simulation and models created in MATLAB® and COMSOL.

This year concluded the development of the thermoelectric measurement device for the FP7 UNION project. The device is capable to carry out the complex task of capturing a micron-size composite cluster of nanoparticles from a solution and measuring electric potential drop across it while exposing it to a temperature gradient. Also, as part of OTKA PD-105173 (A. Deák: Nanochemistry for controlled self-organization), the finite element framework has been used to study the elementary physical components of the interaction of surface functionalized (core-shell) nanoparticles in electrolyte with each other and a potential wall. We attained the

complete thermodynamical description, changes in the Gibbs free energy depending on characteristic geometrical parameters of the 2D or 3D model systems. An example of the electric potential distribution between two nanoparticles is shown in Fig. 2.

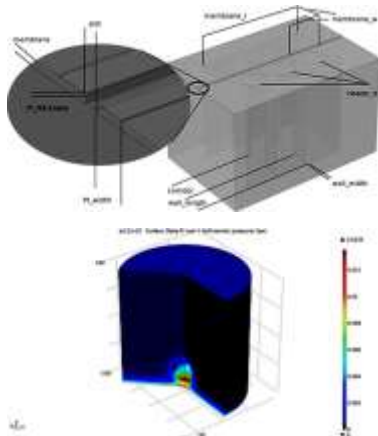


**Figure 1** Schematic view of the parameters of the UNION micro-thermoelectric measurement device.

**Figure 2** Van't Hoff osmotic pressure arising from electrostatic interactions in the electrolyte near a nanoparticle and potential wall.

### 3D interpolated potential for MD

We began development of a novel computational approach, based on multivariate interpolation for a complete and accurate description of three-body interactions in atomic and molecular ensembles. A natural 3-dimensional counterpart of the London dispersion is the so-called Axilrod-Teller-Muto (ATM) potential. For intermediate and large distances, ATM describes the three-body contribution to the energy of interacting particles. When particles (e.g. noble gas atoms) get in the vicinity of each other, quantum-mechanical correlation effects come into domination. Even their approximate (post Hartree-Fock) calculation requires considerable computational resources and time. To make these contributions more available for large ensemble, longer molecular dynamics (MD) simulations, a proper twice differentiable interpolation scheme was developed and implemented, smoothly fitting also the ATM potential at larger distances.

First test calculations on many-body systems (4, 5, 6 atom random clusters of He atoms) show, that the total interaction (or cohesive) energy of these can be very closely approximated by the sums of 2 and 3-body contributions. Fig. 3 shows the example of He-4 clusters.



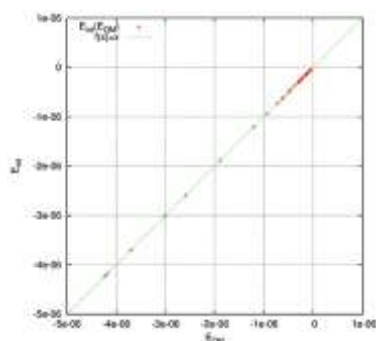


**Figure 3** Comparison of the interpolated and "exact" (QM) cohesive energies of random He-4 clusters. The diagonal (green) line means perfect correspondence, which the red points fall indistinguishably close to.

### Nanosize effect on the evolution of magnetism on curved surfaces

Similarly to the well-known Moore's law for the number of transistors in an integrated circuit, an analogous tendency was recognized by Mark Kryder for magnetic disk storage density. His prediction shows that the capacity of a 2.5" disk will reach 40 TBit/ in<sup>2</sup> by 2020. Several developments are now on the way in order to reach, or even to exceed this density.

There are two dilemmas about storage capacity increase. Once, when the magnetic grains are very small, the further reduction leads to the super-paramagnetic effect, where the spontaneous magnetization fluctuation results in data loss. On the other hand, the magnetostatic and exchange interaction between the adjacent grains sets a limit on how "strong" the magnetization should be in a grain without being perturbed by the neighbors.

A possible solution could rely on bit patterned media where the information unit is bound to a nanostructure. In this case the strong exchange coupling within the particle, the shape anisotropy and the isolation of the particles may increase the energy barrier for thermal switching. Such structures are predicted to be eligible to store up to 20-300 Tbit/in<sup>2</sup>. As material properties may differ from bulk when entering the nanoscale regime and this is particularly true for magnetic materials, scientists from all over the world are working to reveal the nanosize effects on magnetism. Our institute EK MFA is also participating in this challenge in cooperation with the ESRF group at the Nuclear Resonance Beamline ID18, the KU Leuven, and the Wigner Research Centre in Budapest.

In this work, an ultrathin iron film was deposited by molecular beam epitaxy (MBE) on a flat silicon substrate as well as on 20 nm and 400 nm diameter silica spheres (Fig. 1), and the effect of morphology such as curvature and interparticle distance, on the evolution of magnetism was studied. The thickness of the iron film was varied in the range where iron shows a nonmagnetic/magnetic transition. To describe the 3D structure, the composition and the magnetic properties of the samples a wide range of analytical tools has been applied such as in situ nuclear forward scattering (NFS), X-ray reflectivity (XRR), grazing-incidence small-angle X-ray scattering (GISAXS) and

ex situ atomic force microscopy (AFM), magnetic force microscopy (MFM), field electron scanning electron microscopy (FESEM), and Rutherford Backscattering Spectrometry with 3D structure evaluation tool (3D-RBS). Based on the detailed characterization, micromagnetic simulations were carried out to model the magnetic moment configurations in the iron cap (Fig. 1).

We concluded that for the two particle diameters largely different evolution of magnetism occurred with increasing the iron thickness. For the 400 nm diameter spheres, the system could be considered as a sum of individual magnetic particles. Here the formed magnetic structure was determined by the topology of the spheres. With increasing the iron thickness, first the upper part of the sphere became magnetic, showing a spiral like (vortex) magnetic pattern on top and out of plane magnetization at the side. For thicker iron layers the out of plane component was gradually eliminated and replaced by a magnetic vortex (Fig. 1b).

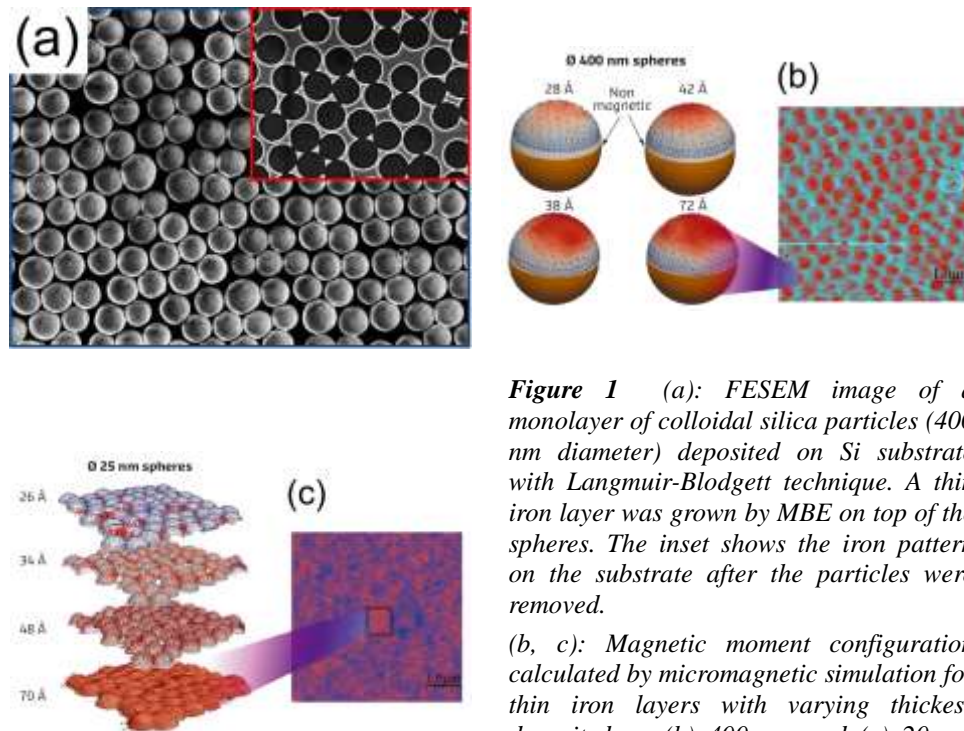


**Figure 1** (a): FESEM image of a monolayer of colloidal silica particles (400 nm diameter) deposited on Si substrate with Langmuir-Blodgett technique. A thin iron layer was grown by MBE on top of the spheres. The inset shows the iron pattern on the substrate after the particles were removed.

(b, c): Magnetic moment configuration calculated by micromagnetic simulation for thin iron layers with varying thickness deposited on (b) 400 nm and (c) 20 nm diameter silica spheres. The magnetic force microscopy (MFM) images of the thickest iron layer are also shown.

In contrast, for 25 nm diameter particles, iron became magnetic first in the contact region of the spheres and a uniformly distributed, well isolated magnetic structure appeared. With further deposition, the whole layer became magnetic and a topology

---

independent magnetic structure incorporating several particles with in plane magnetization could be observed (Fig. 1c).

## **BioMEMS**

**Activity leader: P. Fürjes**

**Group members:** Zs. Baji, I. Bársony, P. Földesy, Z. Hajnal, A. L. Tóth, V. Rakovics, I. Réti, E. Holczer, and E. Tóth

### **Projects:**

- ENIAC CALL 2013-1 – “Intelligent Catheters in Advanced Systems for Interventions – INCITE”
- OTKA CK 83821 – “Mikrocsatornák készítése protonnyalábos mikromegmunkálással és alkalmazásuk Lab-on-a-chip eszközökben”
- KTIA VKSZ\_14 – “Multiparaméteres Point of Care in vitro diagnosztikai rendszerek fejlesztése”
- EURIPIDES / EUREKA 13-1610 – “Particle Matter sensors for indoor air quality – PAMIAQ”

### **Microfluidic system for separation of circulating tumor cells (CTC)**

Cell sorting could have particular importance in medical diagnostics and therapy – see Clinical Cancer Advances – since it can be applicable to select specific cell types or to remove the background cells from such important and limited volume biological samples as taken from blood or liquid biopsy. Microfluidic Cell Capture Devices (MCCDs) are promising tools for detection, capture and enrichment of the targeted cells since the geometrical dimensions of the cells and the applied channels are in the similar order of magnitude. Due to their small dimensions (with the benefit of high surface to volume ratio), they can offer unusual physical behaviour that is in the macroscopic world.

The specific aim of this project is to design and fabricate microfluidic cell capture devices with special 3D geometry utilizing the advances of combining conventional lithography based rapid prototyping with Proton Beam Lithography (PBW) to improve cell manipulation efficiency. Tilted micropillars were fabricated and applied in order to increase the active surface area, the effective cross-section of the capturing microstructures and to modify the local hydrodynamic behaviour in the sample transport system, in cooperation of the research groups of Prof. A. Guttman (Univ. of Pannonia) and I. Rajta (ATOMKI).

Computational Fluid Dynamics (CFD) simulations revealed that tilting the pillars not only increases their surface area on which the fluid can interact with the bonded affinity layer but also improves the fluid characteristics of the system. Based on the results of the preliminary FEM calculations special 3D structures were designed and fabricated by multiple tilted proton beam writing method in SU-8 epoxy based

negative photoresist and poly-dimethylsiloxane (PDMS) to enhance the cell capturing capability of the proposed microfluidic system. The developed 3D microstructure of the microfabricated cell separation system was imaged by scanning electron microscopy as demonstrated in Fig. 1.

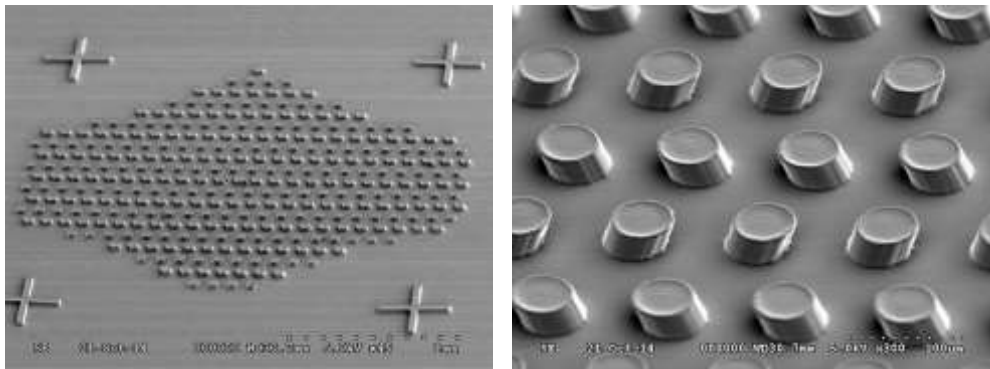


**Figure 1** SEM images of doubly tilted micropillars fabricated from liquid PDMS by polymerization with focused proton beam on the top of a cross-linked PDMS layer.

The presented methodology and the applied structural materials are compatible with MEMS/NEMS (micro/nano-electromechanical systems) technology considering the integration requirements for subsystem development. The PBW patterned micropillar array was integrated into the transport microfluidic system manufactured by soft lithography and its performance was characterized by cell injection. The sealed device is presented in Fig. 2.

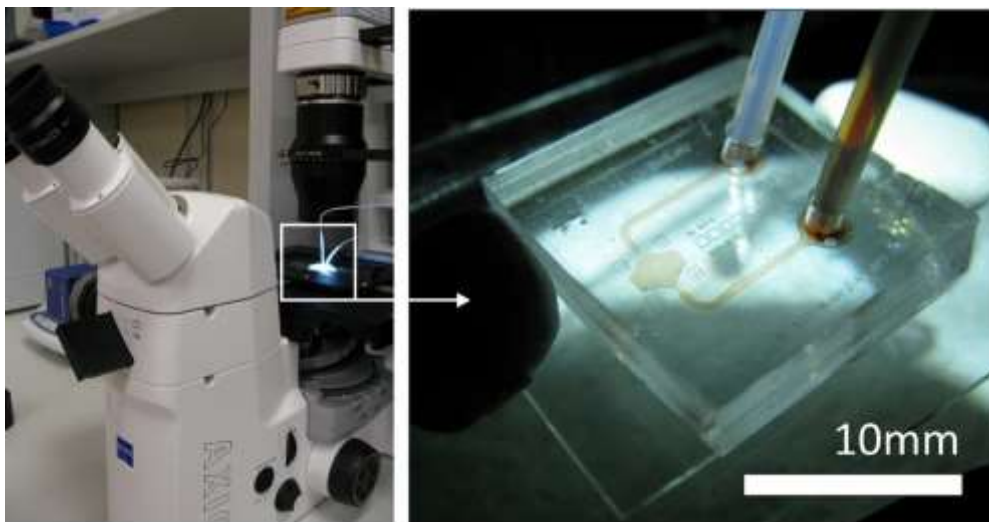


**Figure 2** The fabricated cell capturing device sealed by  $O_2$  plasma enhanced bonding of the microfluidic and sorting subsystems was filled by biological test solution containing yeast cell culture.



To validate the FEM modeling of the hydrodynamic processes evolving in the cell capturing chamber, the particle movements were monitored in the fabricated microfluidic system by using fungi cells in typically similar size of red blood cells. The cell trajectories were monitored and followed by microscopic imaging. The experienced deterministic lateral displacement is governed by the asymmetric local hydrodynamic characteristics evolving around the tilted pillars. The particle behaviour corresponds to the FEM modeling results clearly demonstrating the asymmetric pressure and shear force distribution near by the tilted micropillars. These satisfied the expectations that the device is capable for size dependent sorting of injected objects and the microfluidic system is offering advanced cell capturing capability at the functionalized surfaces.

### **Finite Element Modeling (FEM) and characterization of cell and molecular advection in continuous microfluidic systems**

The aim of the research is the characterization of the fluid-particle interaction in biological samples (blood, environmental samples, etc.) considering cellular and molecular advection and implementation of targeted preparative functions on microscale. Considering the main sample preparation tasks the behaviour of particle- and cell suspensions in the microfluidic systems was analyzed focusing on the separation of the formed elements and particles by size.

Several medical diagnostic tests are based on human blood as sample solution due to its complex and representative marker molecule composition considering pathological issues. Most of these tests require separation of plasma or serum from the whole blood. Recent development of microfabricated Lab-on-a-Chip systems provides outstanding solutions for analytical problems although integration of high performance continuous separation function is challenging. Passive microfluidic inertial plasma separation structures could be promising candidates due to their relatively simple structure and fabrication technology. Zweifach-Fung bifurcation type microscale separation systems utilize viscous lift and shear forces evolving in the low Reynolds regime and developing a cell-depleted layer near the channel walls. This structure could provide excellent plasma purity in single branch, however, in case of cascade separation systems purity is deteriorated subsequently from branch to branch due to the thinning of the cell-depleted layer. In our work the possible recovery of the cell-free layer was studied considering inertial forces evolving in special geometrical singularities.

#### **Characterization of cascade plasma separation structures**

Series of different geometric singularities (six types of different expansions) were integrated with bifurcations branching from main stream channel in order to reveal their inertial effects on particle movement and characterized regarding their enhancement of blood plasma separation performance of cascade Zweifach-Fung bifurcations. The evolving flow behavior and particle trajectories were modeled by



Computational Fluid Dynamics (CFD) simulation and particle tracing modules of COMSOL Multiphysics and the results were verified experimentally by recording particle trajectories. Microfluidic test structures were fabricated by soft lithography in poly-dimethylsiloxane (PDMS) and fungi cells were injected in to reveal particle movement applying dark field microscopy. The modeled flow fields were compared to the recorded particle trajectories in case of different flow rates (Fig. 1).

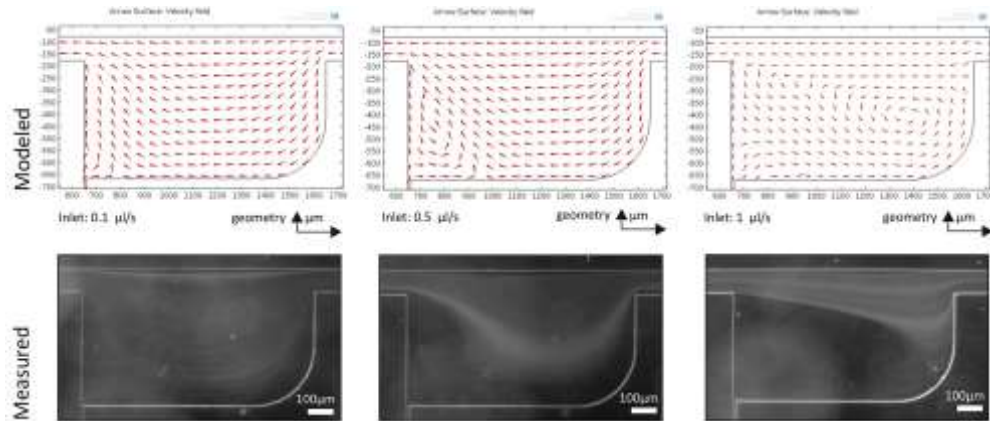


**Figure 1** Modeled flow velocity fields in a representative singularity in case of different injected flow rates compared to the experimentally recorded particle trajectories.

Both simulation and experiment proved the development of the cell-depleted layer due to the applied series of singularities as demonstrated by the modeled particle distribution and the recorded backscattered intensities in Fig. 2.

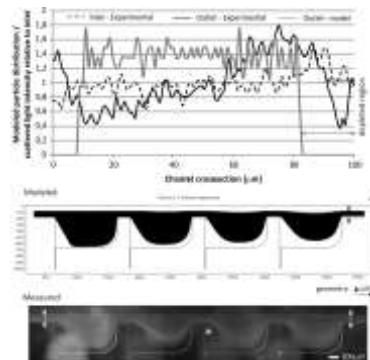


**Figure 2** Modeled and experimentally recorded particle trajectories representing the development of depleted layer. The particle distribution and the measured scattered light intensities demonstrate the effect of lateral migration.

The development and recovery of a cell-depleted layer near the channel walls due to lift and shear forces were analyzed considering the applied flow rates and number of singularities. To avoid deterioration of plasma purity due to cell recirculation in evolving vortices but maximize separation efficiency optimal flow rate regime was defined for further experiments. The recovery of the cell-free layer in geometrical singularities was validated and their applicability in enhanced cascade type plasma separation systems was proposed. The effect of the developing cell-depleted layer thickness on the plasma purity was studied to prove the improvement of the separation technique due to the integrated inertial subsystems.

## Autonomous microfluidic sample transport systems

Autonomous capillary micropumps could be substantial brick stones of cheap, simple and self-powered microfluidic systems being capable to manage the sample transport in Lab-on-a-Chip applications. Accordingly the precise control or improvement of the fluid conducting characteristics of these integrable micropumps is in forefront considering their capacity and efficiency. Moreover the management of the achievable flow rate and the transported sample amount could be critical regarding various applications considering the requirements of controlled microreactors or high sensitive diagnostic devices, and the transported amount has to be adjusted by the geometric and surface parameters of the developed passive pump.

### Development of self-driven microfluidic systems

To achieve controlled and autonomous sample transport in Polydimethylsiloxane (PDMS) based microfluidic system the surface behaviour of the material was modified, and the efficient transport of patient serum was proved. Since the functionality of the proposed biosensing/Lab-on-a-Chip device is highly affected by the flow conditions during the sample injection, incubation and washing steps, microfluidic chamber system was developed to ensure controlled transport of the sample suspension over the biosensing surface by capillary forces. The microfluidic structure was fabricated by soft lithography technique in PDMS using SU-8 epoxy based photoresist as **molding** replica. The PDMS was modified to improve its sample transport performance by embedding special PDMS-b-PEO amphiphilic molecules in the matrix.

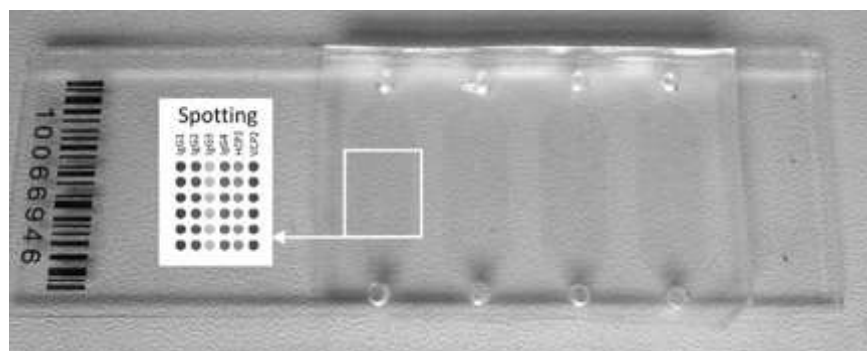


**Figure 1** The fabricated PDMS based microfluidic chamber.

### Biosensing applications

In cooperation with the ELTE/MTA Immunology Research Group the developed self-driven polymer based microfluidic system was applied for a biosensor to be able to monitor immune cell adhesion and activation on protein microarrays consisting of antigens, antibodies and complexes indicating specific autoimmune diseases. Cells as biosensors were applied for monitoring immune complex composition. When the capillary system was mounted above the slide, first serum samples derived from



patients then purified human neutrophil granulocytes were transferred through the capillary system by capillary force. Applying the adequate peptide targets of specific autoantibodies, the adhesion of neutrophil granulocytes on the functionalised surface regions clearly indicated the diseased patient sample. The readout of the assay can be the quantitation of bound fluorescently labeled cells by a microarray scanner as schematically represented in Fig. 2.

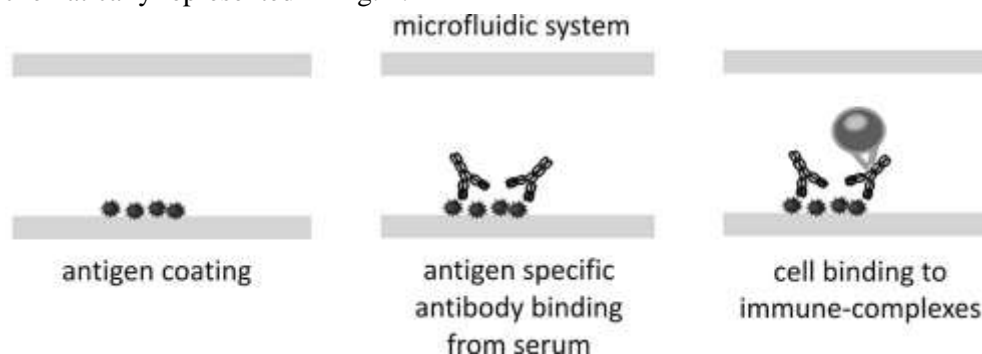


**Figure 2** Schematic working principle of the cell-binding biosensor assay for detection antigen specific antibody in the patient serum.

We proved that the capillary driven microfluidic transport system applied for filling the sample chambers of microarrays can significantly improve the effective cell binding and the ease of handling and reproducibility of these assays in diagnostics of disease positive patients.

### Complex bioinspired microcapillary systems

The functional behaviour of the capillary structures and the non-specific protein binding on the channel surfaces were also studied to prove the auspicious effect of the surface modification. The geometry and the 3D design of the channels were inspired by the most complex natural microfluidic system, the water-conducting tissue (xylem) of trees and different geometric shapes were developed at the bottom of the channels as stripe and serpent type grooves. The combined effects of different 3D geometries and surface modifications were systematically characterized by flow rate measurements applying ultra fast imaging system for recording fluid movement. The surface modification methods were compared and the advantages of bioinspired capillary systems were also demonstrated.

Bioinspired microfluidic structures as fluidic diodes were also designed and characterized to systematically control the sample flow rate and direction in the microcapillary systems. 3D geometry of the skin of Texas Horned Lizard was adopted and proved for flow direction control in autonomous sample transport systems. Based on the preliminary result autonomous sample transport microfluidic systems were designed and fabricated to be integrated in Point-of-Care Lab-on-a-Chip based diagnostic cartridges in the cooperation with 77 Elektronika Ltd.

## Cell and particle sorting in microfluidic systems

The aim of the PAMIAQ project in cooperation with Technoorg Linda is the development of a complex analytical system for particle counting and identification by size distribution with integrated sample transport, manipulation and optical detection. Microfluidic systems capable of particle separation by their size utilizing the Dean drive and inertial effects were designed and analyzed. Fluidic chips were fabricated in PDMS by soft lithography and bonded to glass plates. These devices will perform passive separation of the pollutants by their size and the hydrodynamic focusing. The microfluidic devices were characterized with respect to their ability of spatial separation of specific pollutants into sub-channels and focusing of the particles in the field of view of the optical measuring setup maintaining the permeability/capacity of the channels. The size ranges of the targeted pollutants were defined as cells – with diameter under 5  $\mu\text{m}$ , particulates with diameter between 1 and 10  $\mu\text{m}$  and pollen with diameter between 10 and 100  $\mu\text{m}$ .

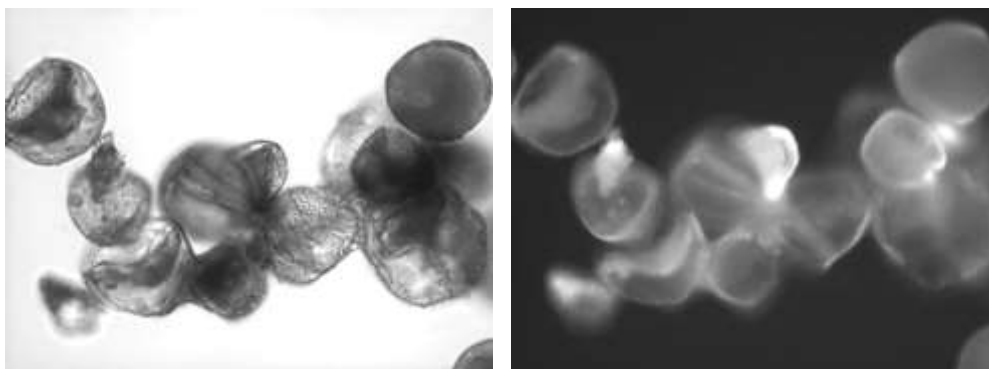


**Figure 1** Tulip pollens visualised by bright field (left) and fluorescent (right) microscopy.

The channel layout design is based on four physical phenomena. Pinched flow fractionation utilizes the inertia of the particles deflecting their paths in varying degrees based on their size. Inertial and Dean forces divert the smaller particles closer to the channel centre and the larger particles towards the channel walls in curved channels. With hydrodynamic filtering the smaller particles can be separated using a comb-like design and a secondary flow.

The mask layout of the combination of fundamental elements was designed, a manufacturing process and measuring method was defined allowing the optical evaluation of the samples. Fluorescent polystyrene beads (10 and 15  $\mu\text{m}$  diameter) were injected into the flow in order to assist optical evaluation. The trajectories of these beads are well defined using fluorescent microscopy.

The combination of Pinched flow fractionation, Dean and Inertial forces was found to be efficient for size dependent particle separation. The hydrodynamic filtering, however were not feasible on the given size scale and technical conditions.

Hydrodynamic 3D focusing was also studied using finite element modeling. The design for the pinched flow fractionation is considered sufficient for the 3D focusing combining the Dean effect with classical 2D hydrodynamic focusing.

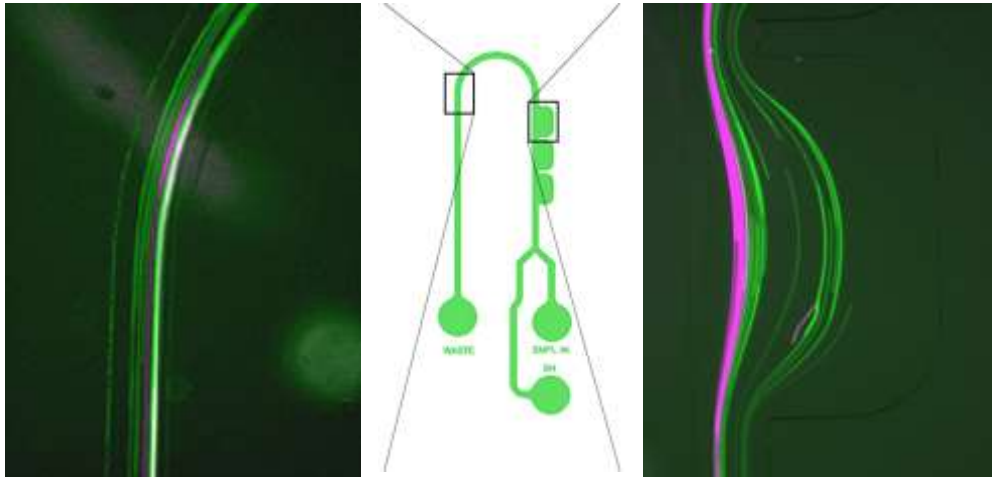


**Figure 2** The size dependent separation of the fluorescently labelled particles were proved by recording their trajectories in the different regions of the microfluidic systems ( $10\mu\text{m}$ : green,  $15\mu\text{m}$ : violet).

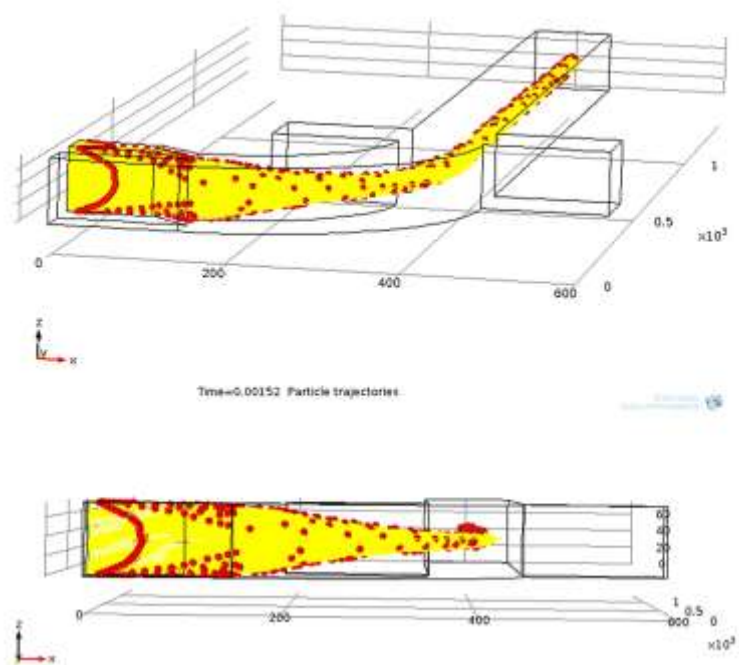


**Figure 3** Finite element modelling of the particle trajectories affected by combined lateral focusing and Dean effects.

## NeuroMEMS

**Activity leader:** Z. Fekete

**Group members:** A. Pongrácz, P. Fürjes, I. Lukács, Z. Hajnal, Gy. Molnár, A. L. Tóth, Z. Bérces, and G. Márton

### Projects:

- Richter Témapályázat – “Memória és az autizmus kutatásában felhasználható, ipari igényeket kielégítő, lokális gyógyszeradagoló csatornával ellátott sokpólusú szilícium alapú in vivo elektrofiziológiai mérőrendszer fejlesztése szabadon mozgó állatokban történő gyógyszer hatóanyag tesztelésére a pre-klinikai fázisban”
- KTIA 13 NAP A IV/6 National Brain Research Program – “NAP A - MEMS érzékelők és beavatkozók vizsgálata agykutatási célokra”
- KTIA NAP 13-2-2015-0004 – “Hippokampális és mélyagyi struktúrák optikai stimulációjának újszerű megközelítései mikro- és nanotechnológiai megoldásokkal”
- TÉT\_14\_FR-1-2015-0030 – “Agyi jelek szerveződési szinteken átnyúló integrált módszertani vizsgálata újszerű elektródával”
- OTKA NN 116550 – “Nanostruktúrák hatásának vizsgálata az idegsejt - szilárdtest kölcsönhatásra agy-gép interfészek fejlesztéséhez”

### Silicon probes designed for infrared neural stimulation

Infrared neural stimulation (INS) was discovered in 2005, when action potentials were successfully evoked using infrared light. Histology was performed after revealing that there is a radiant exposure range, where action potentials are elicited without damage. In our work, a Michigan-type silicon microprobe for infrared neural stimulation was designed and investigated in terms of technology induced surface roughness and optical transmission. The fabrication of such optrode was realized by deep reactive ion etching and subsequent wet chemical polishing.

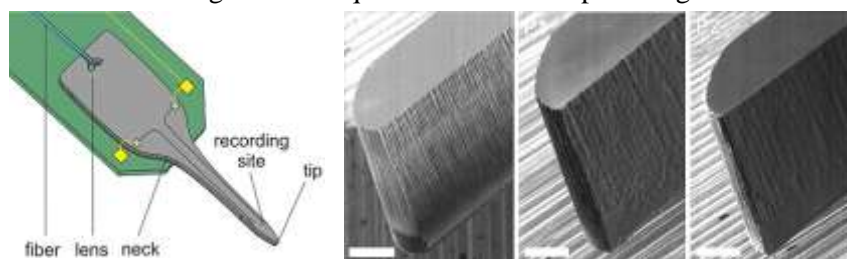


**Figure 1** Concept of a silicon microelectrode that provides infrared stimulation and records the electrical activity of neurons simultaneously (a). Perspective and side view of the microprobe tips. R: reference sample before polishing. P1, P2: polished samples after one and two minutes, respectively. Scale bar is 100  $\mu\text{m}$ .

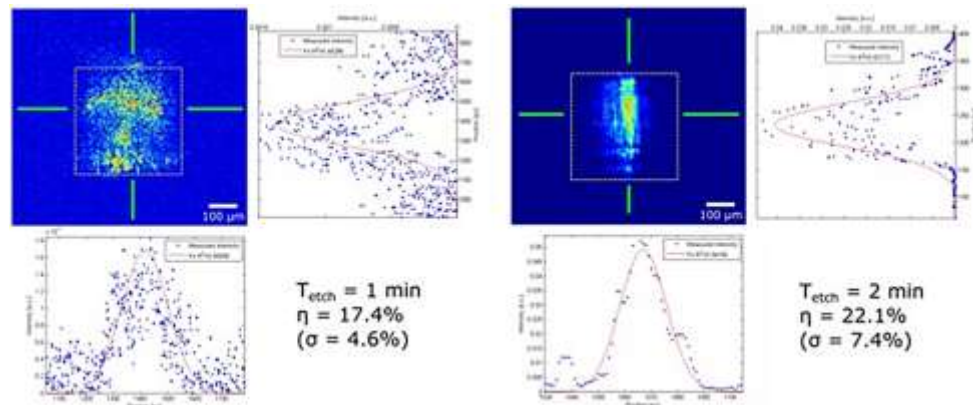


**Figure 2** Beam profile of P1 (a-c) and P2 (d-f). Dashed yellow lines represent the contour of the probe shaft, while green lines indicate the X and Y cross-section of represented data on optical power.

The overall efficiency was further boosted by integrated couplers and focusing microlenses etched into the silicon substrate. Due to the proposed fabrication approach, 22.1% in system efficiency was achieved at a wavelength of 1310 nm. We observed that system efficiency does not increase significantly by increasing the time of sidewall polishing; however, the beam shaping effect of the coupling lens is more remarkable, if the tip roughness is reduced down to 8.7 nm RMS value. The spatial distribution of the delivered light can be also controlled through integrated micromirrors at the probe tip, which facilitates lateral out-coupling with a Gaussian beam profile.

### **Iontophoretic injection microsystem delivering pathway tracer molecules in the living tissue**

Exploring the structure and function of the brain's connectome is in one of the major scope of recent neuroscience research. Complementing neuronal recording with pathway tracing is still an indispensable tool to achieve such goals specifically at the microcircuit (single neurons) and mesoscale (neuronal populations) levels of the neural network. However, electrophysiology and neuronal tract tracing are usually applied separately even if combined in the same experiment. In our work, we present the results of *in vivo* local release of a neuronal tracer, biotinylated dextran amine (BDA) in the rat somatosensory cortex using monolithically integrated microfluidic channel of a silicon neural microelectrode. The tracer injection is controlled by iontophoresis using Pt electrodes in the vicinity of the outlet of the microfluidic channel. Using 3-5  $\mu\text{A}$ , 5-7 s on/off cycle and 15-20 min total injection time the localized injection resulted in clear anterograde and retrograde BDA labeling both within the cortex and in subcortical structures. Anterograde and retrograde labeling revealed the fine details of neuronal processes including dendritic spines and axon

terminal-like endings. Injection sites appeared clear lacking any strong diffuse background labelling. Electrophysiological recording performed with the same microdevice immediately after the iontophoresis indicated normal cortical functioning. The results prove that the combination of in vivo multichannel neural recording and controlled tracer injection using a single implanted microdevice is feasible, and therefore it can be a powerful tool for studying the connectome of the brain.

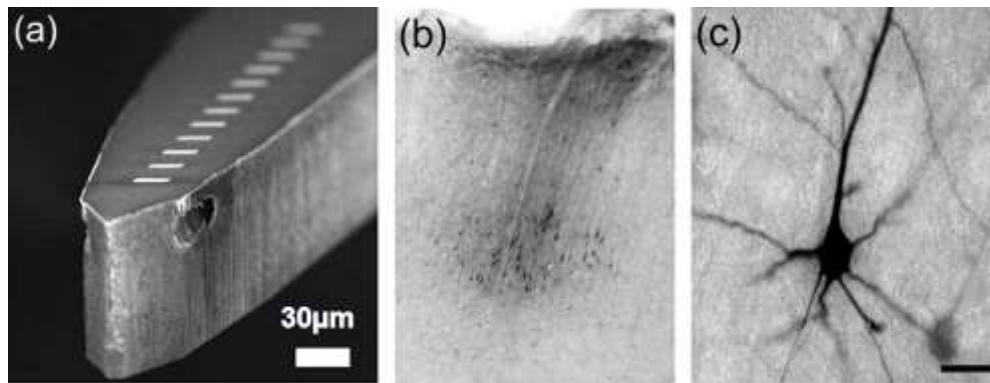


**Figure 1** (a): SEM image of a silicon neural electrode with 12 Pt contact sites on the top surface and two buried microfluidic channels. The outlets of the channels are on the sidewalls. Contact closest to the outlet serves as counter electrode during iontophoresis, while the reference electrode is placed in the microfluidic interface connected to the probe. The remaining contacts are applied for electrophysiology. (b): BDA labeled neuronal cell bodies (black dots) are present all along the electrode track and accumulate in the deep layers. Note the lack of a dense tracer deposit and that the labeled neurons are clearly distinguishable. (c): Close view of a both anterogradely and retrogradely labelled neuron.

## Polymer microECoGs optimized for in vivo pharmacological investigations

The connectivity between the cortical representations of the visual system through temporary oscillations plays an important role in the pathomechanism of the so-called connectome diseases like schizophrenia or autism. The complexity of the visual cortex makes it difficult to find a reliable electrophysiology technique, which is able to measure the electrical activity of the whole cortical connectome simultaneously. Our goal was to elaborate a chronically implantable polymer based microelectrode grid that is able to monitor large cortical areas in rodents. The feasibility of the subdural electrode system was tested in visual steady-state response experiments, in ketamine induced schizophrenia models and in 4-aminopyridine induced epilepsy models using mature Wistar rats. Our results prove the potential of our microelectrode grid system in future pharmacological research.



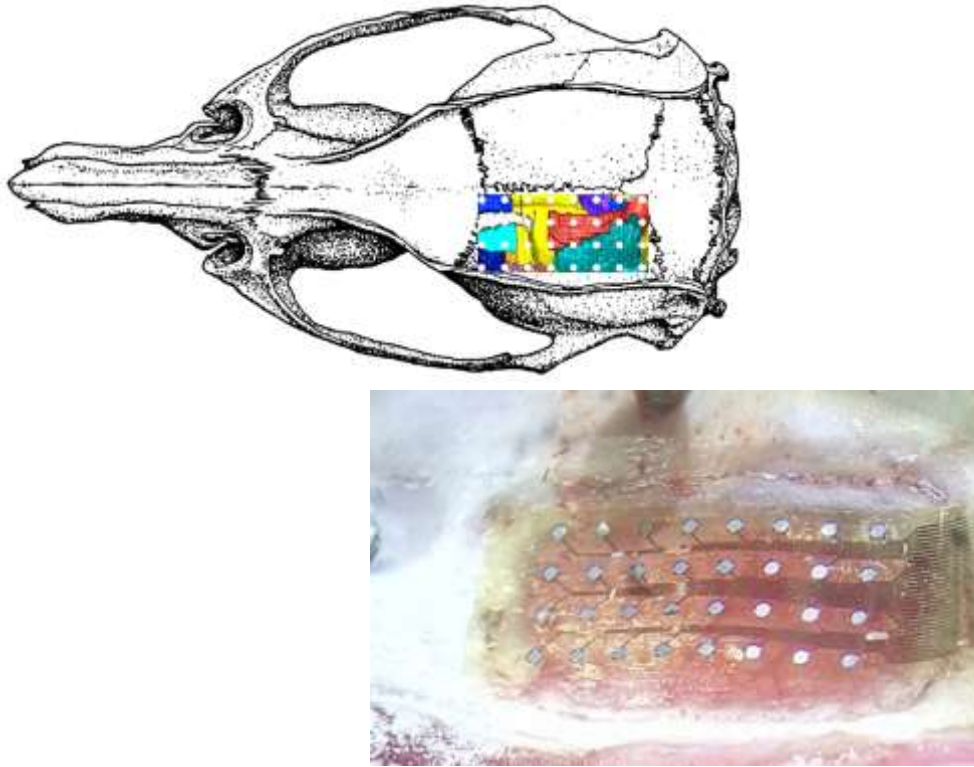


**Figure 1** Schematic of rat skull with the implantation sites of the microgrid (left). Our polymer microgrid during surgery (right).

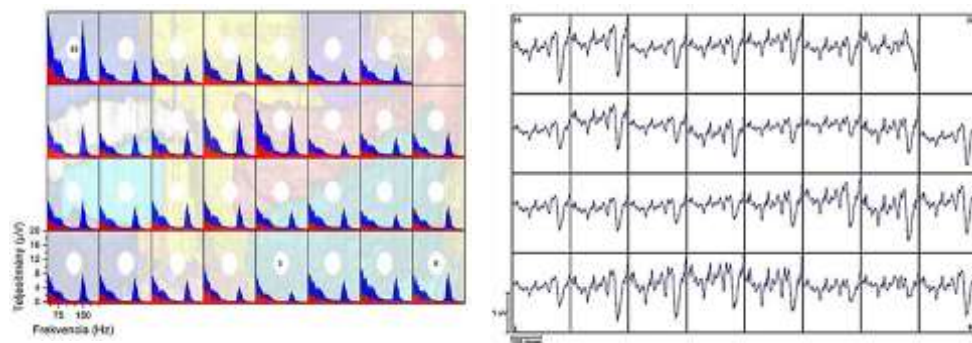


**Figure 2** Ketamine induced dissociation state in schizophrenia animal model. Red and blue area represent spectral power density in a control period (10s) and after ketamine injection (10s). Measurements were using a 32-channel microelectrode grid directly placed on the visual cortex. Fig. 4: EEG recorded by our microgrid during an epileptic seizure after 4-AP injection.

## In vitro studies revealing the immune response of the living tissue to nanostructured implant surfaces

Our goal is to design and fabricate nanostructured surfaces to reduce the extent of glial cell encapsulation of Central Nervous System implants and to promote neural attachment and regeneration, which improve the biocompatibility and functionality of the interfaces. Recent findings showed that specific glial cells prefer flat surfaces over nanostructured ones with certain geometries, while neural cells proliferate both on nanostructured and flat surfaces.

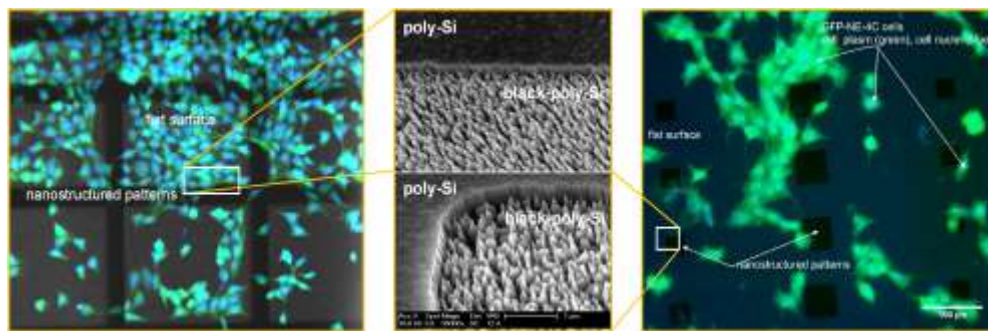


**Figure 1** Two channel fluorescent images of GFP-NE-4C cells on nanostructured chips after 24h adhesion (blue channel: DAPI staining - cell nuclei; green channel: green light is emitted by the GFP expressed in the cytoplasm). Black regions are the nanostructured patterns on the samples. Inset images show the transition region, where flat poly-Si regions meet the nanostructured Si grass. Nanostructured surfaces are less preferred by the NE-4C cells compared to flat regions.

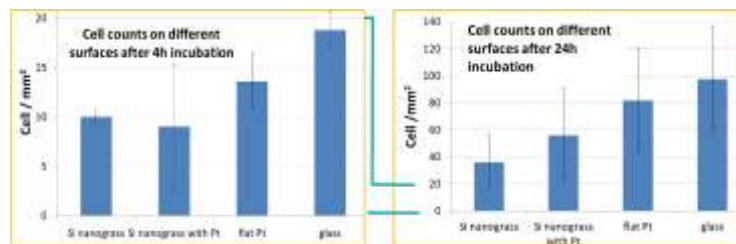


**Figure 2** Comparison of cell counts after 4 hr and 24 hr long incubation of NE-4C neural progenitor cells on different surface types (nanostructured Si, nanostructured Pt, flat Pt and glass). Nanostructured regions hinders the adhesion of the stem cells compared to their flat references.

Neural progenitor cells were cultured on flat and nanostructured Si and Pt surfaces. Based on the MTT tests, the nanostructured surfaces are non-toxic compared to the glass surfaces. Cell adhesion was hindered by the nanostructured surfaces compared to the flat ones. Analysis of fluorescent microscopy images suggests that the cell number increases on every investigated surface type (Si nanoglass, Pt, nanostructured Pt, glass), however, the proliferation is slower on nanostructured regions.



## **NEMS**

**Activity leader: J. Volk**

**Group members:** Zs. Baji, G. Battistig, Cs. Dücső, P. Földesy, N. Q. Khánh, I. Lukács, Gy. Molnár, A. L. Tóth, Zs. Zolnai, R. Erdélyi, Z. Szabó, and I. Bársony

### **Projects:**

- OTKA K108869 – “Széles tiltott sávú félvezető anyagok, nanoszerkezetek és korszerű eszközök”
- OTKA K112114 – “Kombinált mikro-nanotechnológiai eljárások és ellenőrzésük lokális analitikai technikákkal: a mintázatképzéstől az alkalmazások felé”
- FP7-ICT-2013-10- 611019 – “High-resolution fingerprint sensing with vertical piezoelectric nanowire matrices (PiezoMAT)”

## **Homogeneous transparent conductive ZnO:Ga by ALD for large LED wafers**

Transparent conductive oxides are widely used in photovoltaics, thin film transistors and light emitting devices. The most common TCO material is indium doped tin oxide (ITO), but in the past decades the price of indium has been rapidly increasing. One of the most promising replacements due to its excellent transparency in the visible wavelength range and similar electrical conductivity is highly n-doped zinc oxide. Ga doped ZnO (GZO) has an excellent transparency and low resistivity combined with an electrical stability at elevated temperatures and excellent crystalline properties. Atomic layer deposition (ALD) is a promising candidate to produce high quality GZO layers at relatively low temperatures (300 °C) and at large wafer sizes as well.

We used atomic layer deposition to acquire a series of GZO thin films with varying nominal Ga concentrations. Homogeneity tests were carried out on GZO thin films deposited on a 4” glass wafer. The effect of the annealing and the fabricated devices were investigated on GZO layers deposited on a commercial InGaN/GaN LED-wafer, whereas for electric and electroluminescence measurements fully processed GZO coated LED-chips were used. We also tried a number of different thermal annealing processes to gain a film with properties optimized for LED applications.

To find the optimal concentration, GZO/c-sapphire films with Ga concentrations of 1, 2, 3, 4, 5, and 10 at% were used. According to the Hall measurements, the increasing doping level reduces the specific resistivity of the layers down to  $3.3 \times 10^{-4} \Omega\text{cm}$  at 3 at% then it increases monotonously with the growing doping concentration. This behavior is governed mainly by the change in free carrier concentration: The doping increases the free carrier concentration up to  $1.38 \times 10^{21} \text{ cm}^{-3}$ , until reaching an optimal Ga content of 3 at%. In this regime the volume concentration of Ga is close to

the free carrier concentration, which indicates a nearly perfect, uncompensated substitutional doping at Zn cation sites (GaZn). In contrast, the electron mobility decreases from 17 to 11  $\text{cm}^2\text{V}^{-1}\text{s}^{-1}$  as the Ga concentration increases from 1 to 10 at%. This can be attributed to the ionized impurity scattering.

The homogeneity of the GZO layers with respect to thickness and conductivity was tested on a 4" diameter glass wafer. As it can be seen in Fig. 1, the wafer scale uniformity of the films was excellent. The relative standard deviation of the average thickness was 2.1 %. As revealed by Eddy current mapping the ALD GZO layer has an average sheet resistance value of  $137.1 \pm 2.7 \text{ Ohm/sq}$  and a relative uniformity of 2.0 % over the wafer (Fig. 1b). By calculating the specific resistivity map as a production of  $t$  and  $R_{\text{sh}}$  we obtain an excellent uniformity of 0.8 % (Fig. 1c).

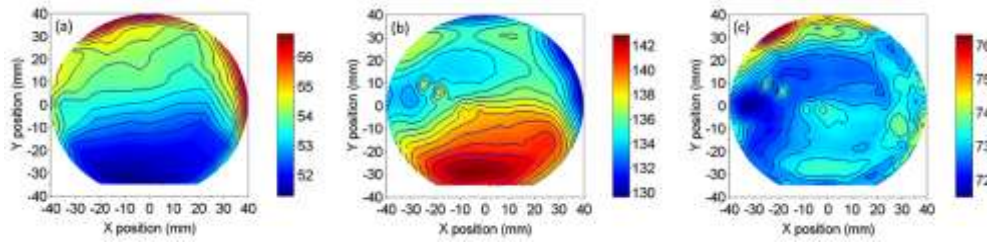


**Figure 1** Thickness (a), sheet resistance (b), and the calculated resistivity map (c), recorded on a limited wafer area in a diameter of 80mm.

For LED operation it is also essential to have a high electrical quality TCO/p-GaN interface with ohmic conduction. In order to address this issue, a proper thermal annealing sequence had to be adopted. We carried out a series of post deposition thermal annealing experiments in the range of 400-800 °C, i.e. above the deposition temperature of 300 °C. Tests by the transmission line method on ALD GZO deposited on commercial InGaN/GaN blue LED wafers were performed. With increasing annealing temperature we found that the I-V curve is gradually improving and becoming fully linear at 700 °C. On the other hand the annealing at such a high temperature deteriorated the bulk conductivity of the GZO films. Therefore we introduced an ‘interrupted growth by ALD’ method i.e. the annealing was performed on a thin ALD grown buffer-layer (of ca. 15 nm). The deposition of the missing thickness followed after that by a second ALD step. This two-step deposition scheme resulted in a slightly improved threshold voltage compared to the as deposited one (2.8 vs 2.9 V, at  $I=20 \text{ mA}$ ), which is even more prominent at higher currents (20-100 mA) (blue vs. black solid line in Fig. 2.). More importantly, the two-step annealing treatment led to a ca. 40-times enhancement in electroluminescence intensity at a driving current of 20 mA (blue vs. black dashed line in Fig. 2).

As a conclusion, ALD proved to be a promising candidate for the deposition of Ga doped ZnO films for LED applications. The 3% doped GZO films have excellent electrical properties, and an annealing treatment can also optimize the quality of the GZO/p-GaN interface.

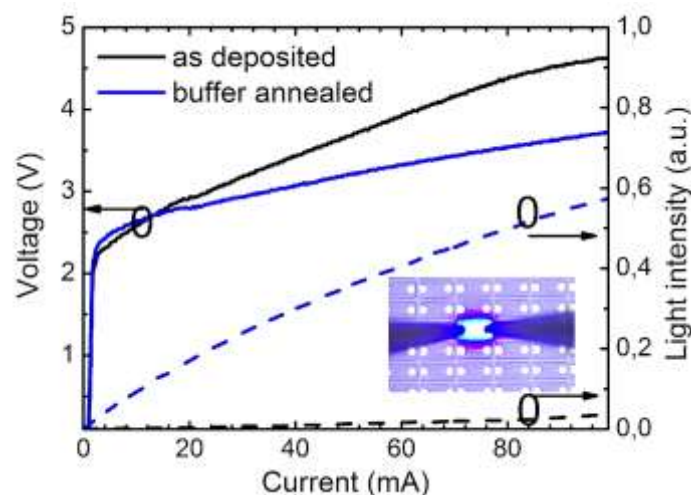


**Figure 2** Voltage (left vertical axis) and output electroluminescence intensity (right vertical axis) as a function of driving current recorded on the LEDs for the thin (ca. 45 nm) non-annealed (black) and 2-step deposited annealed GZO TCO (blue), respectively.

### Double Markers for Direct Contact Formation on Ultra-Low Dimension Objects

For contact formation on very small objects, like  $\text{TiO}_2$  nanowires (NWs) with ultra-low dimensions (few nm wide and few tens nm long), determination of the coordinates of the objects in a pre-deposited marker array is a challenge. Thin NWs are hard to see by Scanning Electron Microscopy (SEM), because of weak contrast. Also, the sample becomes contaminated fast at such high SEM magnification.

So far, we carried out very thin metal contact pairs formation with very narrow gap (few tens of nm) to avoid the problem mentioned above. Then Atomic Force Microscope (AFM) has been used to find the adequate NWs, which were accidentally contacted at both ends. Later on, the second metal is to be deposited to make a connection between the leads and the contact pairs. This approach therefore, is very time-consuming due to large number of AFM measurement. Also, the NW's location to the contact is not well controlled. With the new facility (RAITH 150), we have developed a novel technique, where we use a double marker array to enable the contact formation directly on a selected NW.

In our new approach, the thick markers are used to give sufficient contrast of SEM image for alignment at e-beam lithography, while the thinner ones ensure fast determination of the wire coordinates by AFM. The main steps of the procedure are followings:

- Thick marker formation by e-beam lithography and metal deposition. Markers are exposed during alignment procedure, so the thick markers ought not to be located close to the object to be processed
- Thin marker formation with alignment on thick markers
- AFM measurement at thin markers
- Object selection and contact design based on the AFM images
- Contact formation using thick markers

Despite of uncertainties (errors at thick marker alignments, drift in AFM measurements), the results of all NWs of the batch (8 NWs) are acceptable as seen on Fig. 1.

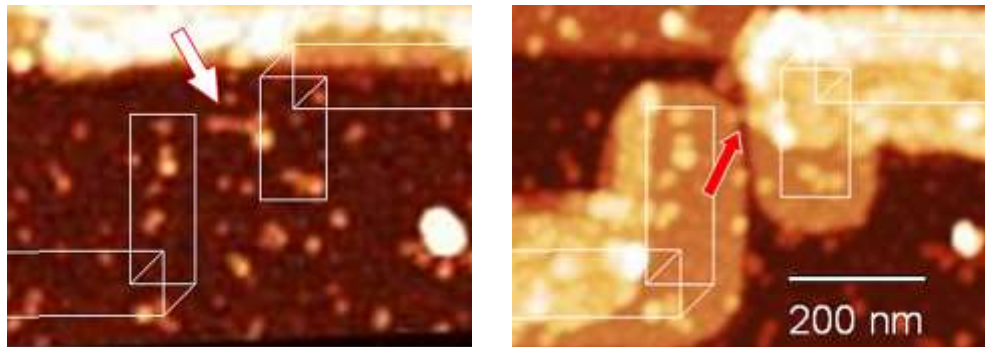


**Figure 1** AFM image of the NW to be contacted indicated by the arrow, the contact design is also shown. Part of the thin marker can be seen on the top of the image (left). Contacted NW with ca. 24 nm gap (right).